Monthly Notices
of the
ROYAL ASTRONOMICAL SOCIETY

MNRAS **491,** 4294–4309 (2020)
Advance Access publication 2019 November 27

doi:10.1093/mnras/stz3319

The impact of the connectivity of the cosmic web on the physical properties of galaxies at its nodes

Katarina Kraljic,[1★] Christophe Pichon,[2,3] Sandrine Codis,[2] Clotilde Laigle,[2] Romeel Davé,[1,4,5] Yohan Dubois,[2] Ho Seong Hwang,[6] Dmitri Pogosyan,[7] Stéphane Arnouts,[8] Julien Devriendt,[9] Marcello Musso,[10] Sébastien Peirani,[2,11] Adrianne Slyz[9] and Marie Treyer[8]

[1]*Institute for Astronomy, University of Edinburgh, Royal Observatory, Blackford Hill, Edinburgh EH9 3HJ, United Kingdom*
[2]*CNRS and Sorbonne Université, UMR 7095, Institut d'Astrophysique de Paris, 98 bis Boulevard Arago, F-75014 Paris, France*
[3]*School of Physics, Korea Institute for Advanced Study (KIAS), 85 Hoegiro, Dongdaemun-gu, Seoul 02455, Republic of Korea*
[4]*University of the Western Cape, Bellville, Cape Town 7535, South Africa*
[5]*South African Astronomical Observatories, Observatory, Cape Town 7925, South Africa*
[6]*Korea Astronomy and Space Science Institute (KASI), 776 Daedeokdae-ro, Yuseong-gu, Daejeon 34055, Republic of Korea*
[7]*Department of Physics, University of Alberta, 412 Avadh Bhatia Physics Laboratory, Edmonton, Alberta T6G 2J1, Canada*
[8]*Aix Marseille Université, CNRS, Laboratoire d'Astrophysique de Marseille, UMR 7326, F-13388 Marseille, France*
[9]*Department of Physics, University of Oxford, Keble Road, Oxford OX1 3RH, United Kingdom*
[10]*East African Institute for Fundamental Research (ICTP-EAIFR), KIST2 Building, Nyarugenge Campus, University of Rwanda, Kigali, Rwanda*
[11]*Observatoire de la Côte d'Azur, CNRS, Laboratoire Lagrange, Bd de l'Observatoire, CS 34229, F-06304 Nice Cedex 4, France*

Accepted 2019 November 15. Received 2019 November 15; in original form 2019 October 17

ABSTRACT

We investigate the impact of the number of filaments connected to the nodes of the cosmic web on the physical properties of their galaxies using the Sloan Digital Sky Survey. We compare these measurements to the cosmological hydrodynamical simulations HORIZON-(NO)AGN and SIMBA. We find that more massive galaxies are more connected, in qualitative agreement with theoretical predictions and measurements in dark-matter-only simulations. The star formation activity and morphology of observed galaxies both display some dependence on the connectivity of the cosmic web at a fixed stellar mass: Less star forming and less rotation supported galaxies also tend to have higher connectivity. These results qualitatively hold both for observed and for virtual galaxies, and can be understood given that the cosmic web is the main source of fuel for galaxy growth. The simulations show the same trends at a fixed halo mass, suggesting that the geometry of filamentary infall impacts galaxy properties beyond the depth of the local potential well. Based on simulations, it is also found that active galactic nucleus feedback is key to reversing the relationship between stellar mass and connectivity at a fixed halo mass. Technically, connectivity is a practical observational proxy for past and present accretion (minor mergers or diffuse infall).

Key words: surveys – galaxies: formation – large-scale structure of Universe.

1 INTRODUCTION

Over the past few decades, the Λ cold dark matter (ΛCDM) concordant model has become a preferred framework in which to interpret when and how the acquisition of physical properties of galaxies occurs. The cosmological model predicts a certain shape for the initial power spectrum of density fluctuations, leading to the hierarchical formation of the large-scale structure, as observed more than 30 yr ago by the first CfA catalogue (de Lapparent, Geller & Huchra 1986). This so-called 'cosmic web' (Klypin & Shandarin 1993; Bond, Kofman & Pogosyan 1996) connects the observed clusters of galaxies via a filamentary network arising from the geometrical properties of the initial density field enhanced by anisotropic gravitational collapse (Lynden-Bell 1964; Zel'dovich 1970). One of the most important features of this framework is arguably to also explain the correlation of many galaxies' properties [kinematics, star formation rates (SFRs)] beyond their mass. The favoured culprit is, unsurprisingly, the interplay between galaxies and the geometry and content of the intergalactic medium in general.

★ E-mail: kraljic.kat@gmail.com

The large-scale environment of galaxies seems to play a significant role in shaping some of their properties, e.g. through torques, while the rest of them are thought to depend mostly on small-scale (internal) processes.

Since the mid-1970s, there have been many studies focused on measuring the impact of environment on galaxy properties. Davis & Geller (1976) first pointed out that late-type galaxies are less strongly clustered than early types, while Dressler (1980) identified a morphology–density relation: Galaxies living in denser environments tend to be redder and have lower SFRs than their isolated counterparts. Since then, a variety of density relations, such as colour–density, star formation–density, and morphology–density relations, have been pointed out by many other works (e.g. Dressler et al. 1997; Hashimoto et al. 1998; Lewis et al. 2002; Blanton et al. 2003; Goto et al. 2003; Baldry et al. 2006; Bamford et al. 2009; Cucciati et al. 2010; Burton et al. 2013; Cucciati et al. 2017, and references therein).

A fundamental requirement to understand such galaxy properties beyond mass is to properly characterize the geometry of their environment, spanning as broad a range as possible, from field galaxies to groups and rich clusters. The vast majority of the studies in the literature accomplishes this task either by counting the number of neighbours of a galaxy within a fixed aperture on the sky or by measuring the distance to the nth nearest neighbour. Although these indicators are easy to obtain, their physical interpretation is far from straightforward (e.g. Blanton et al. 2003; Kauffmann et al. 2004).

A novel approach was introduced by Codis, Pogosyan & Pichon (2018), who focused on the connectivity of the cosmic web network as a means to understand its morphology and geometry. The motivation was two-fold: (i) to characterize the underlying cosmology, since the disconnection of filaments is driven by gravitational clustering and by dark energy, which will stretch and disconnect neighbouring filaments; and (ii) to probe the geometry of accretion on halo and galactic scales. In particular, they showed that connectivity is an increasing function of halo mass, a property that is directly inherited from the underlying density peaks whose connectivity increases with their height.[1] On smaller scales, cosmic connectivity provides a unique view into galactic assembly history, since dark matter filaments typically have a baryonic continuation within dark matter haloes. This closely connects the cosmic environment to the growth of embedded galaxies (e.g. Kereš et al. 2005; Dekel et al. 2009; Kereš et al. 2009). In this context, Darragh Ford et al. (2019) measured the local connectivity, called the multiplicity of connected filaments (Codis et al. 2018), in the COSMOS field around X-ray-detected groups at higher redshifts ($0.5 < z < 1.2$). To do so, they extracted cosmic filaments using the photometric redshifts of the COSMOS2015 catalogue (Laigle et al. 2016) in two-dimensional slices (see also Sarron et al. 2019).

The aim of the current project is to measure the connectivity, both global and local, of the cosmic web in three dimensions (3D), as traced by galaxies in the Sloan Digital Sky Survey (SDSS; York et al. 2000; Ahn et al. 2014), and to study how it relates to the physical properties of galaxies identified as nodes. In particular, we assess the impact of connectivity on the star formation activity of galaxies and the role it may play in quenching star formation. Using a set of cosmological simulations, our aim is, thus, to address the question: At a fixed dark halo mass, to what extent is galactic connectivity a driver of stellar mass, star formation activity, kinematics, or spiral fraction?

The outline of this paper is as follows. Section 2 presents the simulated and observed data sets used in this work. Section 3 presents the local and global connectivity statistics, while Section 4 compares our findings to the connectivity of simulated galaxies. Section 5 investigates the evolution of connectivity and the physical properties of galaxies at a fixed halo mass. Finally, Section 6 concludes. Appendix A presents the impact of persistence on connectivity, while appendix B focuses on the effect of satellites on connectivity. Appendix C contains complementary measurements of the multiplicity. Finally, Appendix D contains complementary measurements in the SIMBA simulation.

In this paper, we refer by the log to the 10 based logarithm. Statistical errors are computed by bootstrapping, with the errors on a given statistical quantity corresponding to the standard deviation recomputed in 100 random samples drawn from the parent sample with replacement.

2 DATA AND METHODS

Let us first describe the data sets and the methods used to characterize the connectivity between observed and virtual surveys. Section 2.1 presents the SDSS catalogue used to compute the filaments, Section 2.2 describes the algorithm used to extract them, while Section 2.3 presents the three hydrodynamical simulations used in the comparison with the observations.

2.1 Observational data

2.1.1 SDSS catalogues

We use spectroscopic data from the main galaxy sample of the SDSS Data Release 7 (DR7, Abazajian et al. 2009). The main galaxy sample includes photometric and spectroscopic data for $\sim 7 \times 10^5$ galaxies at $m_r < 17.77$. However, the spectroscopic completeness for bright galaxies (e.g. $m_r < 14.5$) is poor because of the saturation and cross-talk in the spectrograph, and also for the galaxies in high-density regions, including galaxy clusters, because of fiber collisions. Therefore, Choi, Han & Kim (2010) compiled redshift information from the literature for the galaxies at $m_r < 17.77$ that were missed in the original SDSS galaxy catalogue. We use the Korea Institute for Advanced Study (KIAS) DR7 value-added galaxy catalogue KIAS-VAGC for further analysis.

To reduce the impact of Fingers-of-God along the line of sight, introduced by peculiar motions in galaxy groups or clusters, on the identification of large-scale structures, we use a method similar to the ones adopted in Tegmark et al. (2004, see also Park et al. 2012; Tempel et al. 2014; Hwang et al. 2016). We first run the Friends-of-Friends algorithm with a variable linking length to take into account the fact that the mean galaxy number density changes with redshift in our magnitude-limited sample. As in Tempel et al. (2014), we calculate the mean galaxy separation at each redshift ($d_{\rm mean}$), and adopt the linking lengths of $0.2 \times d_{\rm mean}$ perpendicular to the line of sight and $1 \times d_{\rm mean}$ along the line of sight. These linking lengths correspond to 1 and 5 h^{-1} Mpc, respectively, at $z \sim 0.1$, the median redshift of the sample. We then compare the dispersion of the identified structures perpendicular and parallel to the line of sight. If the dispersion parallel to the line of sight is larger than the perpendicular one, we revise the radial velocities of the galaxies within the structures to have the same velocity dispersion in the two directions.

[1]The higher the peaks, the larger the connectivity because high peaks are more isotropic.

We adopt the SFRs and stellar masses from the MPA/JHU DR7 VAGC. The SFRs are extinction and aperture corrected ones derived from the SDSS spectra. For star-forming galaxies classified in the emission line ratio diagram, they use the Hα emission line luminosity to derive SFRs. For all other galaxies, including AGN-host galaxies where the SFRs cannot be directly measured, the 4000 Å break (D4000) is used for SFR estimates (see Brinchmann et al. 2004 for details). The stellar masses are derived from the fit to the SDSS five-band photometric data with the model of Bruzual & Charlot (2003, see also Kauffmann et al. 2003a). The SFR and stellar mass estimates in the MPA/JHU DR7 VAGC are based on the Kroupa initial mass function (IMF, Kroupa 2001).

The galaxy morphology information is taken from the KIAS DR7 VAGC (Choi et al. 2010). In this catalogue, galaxies are initially classified into two types based on the $(u - r)$ colour, $(g - i)$ colour gradient and i-band concentration index (Park & Choi 2005): early (ellipticals and lenticulars) and late (spirals and irregulars) types. The resulting completeness and reliability for the morphological classification reaches 90 per cent. To complement this automated classification scheme, 13 astronomers in the KIAS group performed an additional visual check of the SDSS *gri* colour images for the galaxies misclassified by the automated scheme. During this inspection, they revised the morphological types of blended or merging galaxies, blue but elliptical-shaped galaxies, and dusty edge-on spirals. It was found that the galaxy morphology in the KIAS VAGC agrees well with that in the Galaxy Zoo catalogues (Lintott et al. 2011; Willett et al. 2013) for ∼81 per cent of the SDSS main galaxy sample.

The classification between the star-forming and passive populations is based on specific star formation rate (sSFR) and sSFR – $M_\star$ cut. Galaxies are classified as passive if their sSFR $\leq 10^{-11}$ yr^{-1} or sSFR $\leq 10^{-10.6}$ yr^{-1} and $\log(\mathrm{sSFR}/\mathrm{yr}^{-1}) \leq -10.7 - 0.2 \times [\log(M_\star/\mathrm{M}_\odot) - 9.5]$ (see Moustakas et al. 2013).

2.2 The cosmic web of the SDSS

In this paper, we measure the connectivity of the cosmic web using the 3D ridge extractor DisPerSE (Sousbie, Pichon & Kawahara 2011),[2] which identifies the so-called skeleton (critical lines connecting peaks together) as 1D-ascending manifolds of the discrete Morse–Smale complex (Forman 2002). This software has been shown to provide a consistent estimate for the connectivity of dark matter peaks (Codis et al. 2018), and to operate well on discrete inhomogeneous galaxy catalogues (e.g. Malavasi et al. 2017; Kraljic et al. 2018; Laigle et al. 2018). This scale-free algorithm relies on topological persistence as a mean to identify robust[3] components of the filamentary network, quantified in terms of significance compared to a discrete random Poisson distribution, through the so-called persistence N_σ.[4] In this paper, all results are shown for $N_\sigma = 3$, unless stated otherwise. We have checked that the choice of the threshold does not alter our conclusions (see Appendix A). Fig. 1 displays the corresponding skeleton constructed from the galaxy distribution.

In DisPerSE, the connectivity is computed automatically: All ridges connecting one peak to its saddles are identified by construction, since the algorithm simplifies specifically components of the tessellation connecting peaks to saddle points using persistence ratios. The number of connected ridges is in practice stored at each node. The multiplicity (or local connectivity) is also straightforwardly extracted from the skeleton via the identification of the bifurcation points of the skeleton (Pogosyan et al. 2009). The multiplicity, μ, is then simply the connectivity, κ, minus the number of bifurcation points associated with each node. Connectivity and multiplicity are complementary since they probe different scales: Connectivity is a measure of the larger-scale topology of the environment, while multiplicity focuses on the number of *local* connected filaments, regardless of whether or not those filaments will bifurcate and split in two or more farther away from the central node. As such, multiplicity is more closely related to the local accretion of matter.

In this work, we consider the properties of galaxies that have been identified by DisPerSE as nodes of the cosmic web, and investigate how they relate to connectivity (global and local).[5]

2.3 Cosmological simulations

In order to make robust predictions for the impact of connectivity on galaxy properties, we examine two independent cosmological galaxy formation simulations, one based on adaptive mesh refinement and the other using a meshless hydrodynamics method. The analysis of these simulations is performed at redshift $z = 0$.

2.3.1 The Horizon-AGN adaptive-mesh refinement cosmological simulation

The Horizon-AGN[6] simulation is described in detail in Dubois et al. (2014). For the sake of the present investigation, we will describe here only the features of interest for the impact of connectivity on the physical properties of the synthetic galaxies.

The Horizon-AGN simulation makes use of the adaptive-mesh refinement code Ramses (Teyssier 2002). The simulation is run in a box size of $L_{\mathrm{box}} = 100\,h^{-1}$ Mpc with a ΛCDM cosmology compatible with the 7-yr *Wilkinson Microwave Anisotropy Probe* data (Komatsu et al. 2011), with dark energy density $\Omega_\Lambda = 0.728$, total matter density $\Omega_\mathrm{m} = 0.272$, baryon density $\Omega_\mathrm{b} = 0.045$, Hubble constant $H_0 = 70.4$ km s^{-1} Mpc^{-1}, amplitude of the matter power spectrum $\sigma_8 = 0.81$, and $n_\mathrm{s} = 0.967$. It contains 1024^3 dark matter particles (i.e. a mass resolution of $M_{\mathrm{DM,res}} = 8 \times 10^7\,\mathrm{M}_\odot$), and the initial grid is refined down to 1 physical kpc. The refinement is triggered when the number of particles becomes greater than eight (or if the total baryonic mass reaches eight times the initial dark matter mass resolution in a cell). A uniform ultraviolet background is switched on at $z_{\mathrm{reion}} = 10$ (Haardt & Madau 1996). Gas cools down

[2]This paper provided a first analysis of all topological components of the SDSS' cosmic web, while Gay et al. (2010) first analysed galactic properties as a function of the distance to filaments and nodes in a cosmological hydrodynamical simulation.

[3]Here robust refers to the topological nature of ridges (see Section 5).

[4]Increasing the persistence threshold allows to eliminate less significant critical pairs and to retain only the most topologically robust features.

[5]In practice, each node of the cosmic web is associated with its closest galaxy. Ideally one should distinguish between centrals and satellites; however, observationally, this is challenging. Since the nodes of the cosmic web are the peaks of the density field, at high mass, picking the closest galaxy often yields the central galaxy. At low mass, however, the bright central galaxy is not always sitting at the centre of mass of the group, and therefore the closest galaxy from the node can be a satellite. This impacts the interpretation mostly at the low-mass end (see Appendix B).

[6]www.horizon-simulation.org

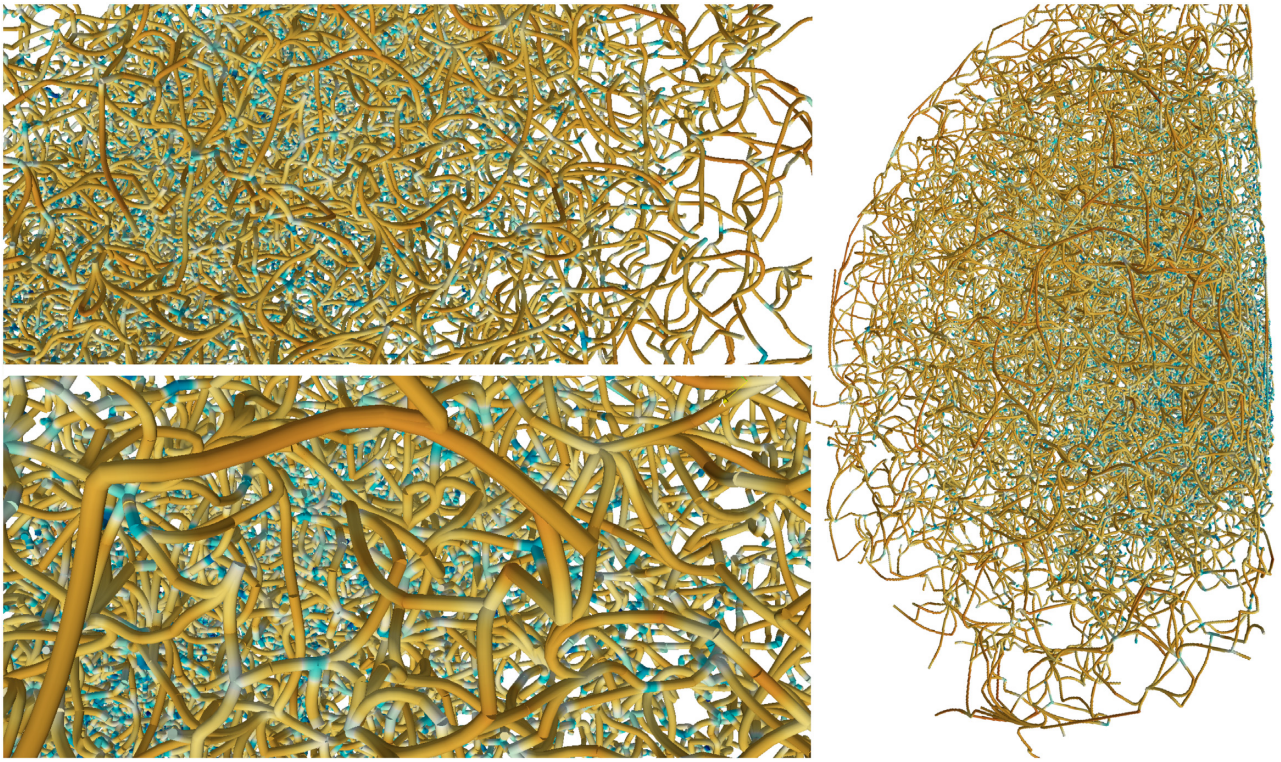

Figure 1. The skeleton of the SDSS DR7 traced by DisPerSE with a persistence level of 3σ from the full galaxy sample at $z \leq 0.19$. Left-hand panel: zoomed-in regions. Right-hand panel: the region over which the connectivity of the network was computed. The colour code traces the underlying density, while the width represents the robustness of the filament. A 3D rendering of the SDSS skeleton can be found at the following URL: http://3dviewer.horizon-simulation.org/3dclouds/SDSS_DR10_segs_graph_points.html.

to 10^4 K via H, He, and metals (Sutherland & Dopita 1993). Star particles are created in regions where gas number density reaches $n_0 = 0.1\,\mathrm{H\,cm^{-3}}$, following a Schmidt relation: $\dot{\rho}_\star = \epsilon_\star \rho_\mathrm{g}/t_\mathrm{ff}$, with $\dot{\rho}_\star$ the SFR mass density, ρ_g the gas mass density, $\epsilon_\star = 0.02$ the constant star formation efficiency, and t_ff the gas local free-fall time. Horizon-AGN implements sub-grid feedback from stellar winds and supernovae (both Type Ia and II). Horizon-AGN also follows galactic black hole (BH) formation and active galactic nucleus (AGN) feedback. When BHs form a tight enough binary, they can grow by accreting gas at a Bondi–Hoyle–Lyttleton rate capped at the Eddington accretion rate. The AGN feedback is modelled as a combination of two different modes, the so-called quasar and radio modes, in which BHs release energy in the form of bipolar jet or heating when the accretion rate is respectively below and above 1 per cent of Eddington ratio, with efficiencies tuned to match the BH–galaxy scaling relations at $z = 0$ (see Dubois et al. 2012, for details).

Galaxies are identified from the stellar particle distribution using the AdaptaHOP halo finder (Aubert, Pichon & Colombi 2004). The local stellar particle density is computed from the 20 nearest neighbours, and are kept when they match the density threshold of 178 times the average matter density (for the dark matter haloes a density threshold of 80 times the average matter density is applied when they contain more than 100 particles). Each galaxy is then associated with its closest main halo.

The impact of AGN feedback on the connectivity of the cosmic web and galaxy properties is assessed by additional analysis of the Horizon-noAGN simulation. This simulation uses identical initial conditions and sub-grid modelling, but does not model black hole formation, nor AGN feedback (Dubois et al. 2016; Peirani et al. 2017).

2.3.2 *The Simba Meshless cosmological simulation*

The third simulation is the Simba simulation (Davé et al. 2019) built on the Mufasa suite (Davé, Thompson & Hopkins 2016). It uses the mass-conserving Meshless Finite Mass version of the Gizmo code (Hopkins 2015). Simba follows the evolution of 1024^3 dark matter particles and 1024^3 gas elements in a volume of 100^3 $(h^{-1}\,\mathrm{Mpc})^3$, with a minimum gravitational softening length of 0.5 h^{-1} comoving kpc, assuming a Planck Collaboration XIII (2016) ΛCDM cosmology with $\Omega_\mathrm{m} = 0.3$, $\Omega_\Lambda = 0.7$, $\Omega_\mathrm{b} = 0.048$, $H_0 = 68$ km s^{-1} Mpc^{-1}, $\sigma_8 = 0.82$, and $n_\mathrm{s} = 0.97$. The initial gas element mass is 1.82×10^7 M$_\odot$, and the dark matter particle mass resolution is 9.6×10^7 M$_\odot$. The volume and resolution are, thus, quite comparable to Horizon-AGN. Radiative cooling and photoionization heating are modelled, including metal cooling and non-equilibrium evolution of primordial elements. A spatially uniform ionizing background switched on at $z_\mathrm{reion} \sim 10.7$ is also assumed from Haardt & Madau (2012), modified to account for self-shielding so that the neutral hydrogen content of gas elements is modelled self-consistently. Star formation is based on the H_2 content of the gas, and the H_2 fraction computation following the sub-grid model of Krumholz & Gnedin (2011) is based on the local column density and metallicity. The SFR is therefore given by SFR $= \epsilon_\star \rho_{\mathrm{H}_2}/t_\mathrm{dyn}$, where ρ_{H_2} is the H_2 density and

$\epsilon_\star = 0.02$. Stellar feedback is modelled via two-phase kinetic decoupled galactic winds, in which 30 per cent of wind particles are ejected 'hot'. Black hole growth is accounted for via the torque-limited accretion model (Anglés-Alcázar et al. 2017) from cold gas and Bondi accretion from hot gas. AGN feedback is modelled via kinetic bipolar outflows. These result in a population of star-forming and quenched galaxies and their black holes that are in good agreement with observations (Davé et al. 2019; Thomas et al. 2019).

Haloes are identified on the fly using a 3D Friends-of-Friends (FoF) algorithm within GIZMO, with a linking length that is 0.2 times the mean interparticle distance. Galaxies are identified using a postprocessed 6D FoF galaxy finder. Galaxies and haloes are cross-matched and their properties computed using the YT -based package CAESAR.[7]

2.3.3 *Galaxy kinematics and properties*

As a proxy for morphology, we use for each galaxy the kinematic ratio of their rotation to dispersion velocity, v/σ, computed from the 3D velocity distribution of stars (as, e.g. in Kraljic et al. 2019). In order to do this, the z-axis of the cylindrical spatial coordinates (r, θ, z) is chosen to be oriented along the total angular momentum of stellar component of the galaxy. The rotational velocity of a galaxy v is defined as the mean of the v_θ of its individual stars, and the average velocity dispersion of the galaxy is computed as $\sigma^2 = (\sigma_r^2 + \sigma_\theta^2 + \sigma_z^2)/3$, with σ_r, σ_θ, and σ_z being the velocity dispersions of each velocity component. While this is not directly comparable to observed measures of v/σ, it allows us to separate rotation-dominated from dispersion-dominated systems (Dubois et al. 2016; Kraljic et al. 2019). The SFR of virtual galaxies in HORIZON-AGN is computed over a time-scale of 50 Myr,[8] while in SIMBA, SFR is computed from the gas particles.[9]

We finally stress that our catalogues (observed and virtual) contain both centrals and satellites, and that we expect the physical properties of these sub-populations to reflect their nature (for instance, starvation, Larson, Tinsley & Caldwell 1980, will operate only on satellites). This effect is investigated in Appendix B, in the context of the stellar mass–connectivity relation.

3 CONNECTIVITY AND MULTIPLICITY IN THE SDSS

Let us now characterize the connectivity and multiplicity (or local connectivity, see Section 2.2) of SDSS galaxies. In Section 3.1, we investigate specifically the impact of stellar mass on connectivity, while Section 3.2 studies the impact of connectivity on the sSFR at a fixed stellar mass.

Let us start by the distribution of multiplicity and that of connectivity. Fig. 2 shows the histograms of connectivity and multiplicity as measured from the full SDSS galaxy distribution in 3D. The medians of these distributions are 3 and 2 for connectivity and multiplicity, respectively. The mean values are fairly similar, 3.26 ± 0.02 and 2.25 ± 0.01, respectively. In this figure, in anticipation of the next section, the measurements from hydrodynamical simulations are also shown as dashed and dotted lines, respectively. Two simulations with different numerical schemes and sub-grid physics are shown in order to get an idea of the modelling uncertainty. The agreement between real and simulated measurements is quite good. Note that these mean values are lower than the predictions for Gaussian random fields (6.1 and 4 in 3D and 2D, respectively). This is expected since here galaxies at all stellar masses are considered, and gravitational clustering and dark energy both disconnect the cosmic web, thus decreasing the connectivity (Codis et al. 2018). With increasing stellar mass ($M_\star \sim 10^{11} - 10^{12}$ M$_\odot$), connectivity starts to grow towards values for Gaussian random field (see Section 3.1). Note also that the low sampling of the field introduces shot noise, which generally tends to disconnect it, as shown on topological estimators like genus by, e.g. Appleby et al. (2017). Since we rely on a discrete galaxy distribution from the simulations, this effect should also be accounted for there. Given that the probability distribution function (PDF) is narrower for multiplicity, thus providing less leverage over environment on larger scales, we will restrict the rest of the analysis in the main text to connectivity, and refer to Appendix C for complementary results on multiplicity.

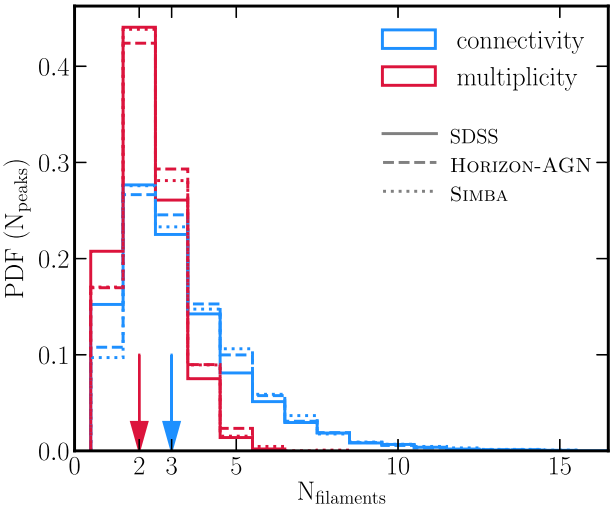

Figure 2. PDF of the connectivity (blue) and multiplicity (red) in the SDSS (solid lines), HORIZON-AGN (dashed lines), and SIMBA (dotted lines). Arrows show medians of the distributions, three for connectivity and two for multiplicity, for all three data sets. See Tables A1 and A2 for mean and median values of connectivity and multiplicity, respectively, as a function of persistence. The consistency between the SDSS and the simulation is remarkable, illustrating the robustness of such estimators.

3.1 Stellar mass dependence

We now consider the variation of connectivity with stellar mass. Fig. 3 shows the connectivity averaged over galaxies in bins of stellar mass, $M_\star$, for the entire population (solid grey line). More massive galaxies are found to have higher connectivity compared to their lower mass counterparts. For the sake of quantifying our

[7] caesar.readthedocs.io

[8] We do not attempt to match exactly this criterion to the SDSS derivation of the SFR, where for normal star-forming galaxies, this is based on the Hα emission (see Section 2.1). The corresponding time-scale is $\sim$10 Myr (e.g. Kennicutt & Evans 2012), which is comparable to the one adopted in the simulations. However, we have also tested shorter and longer time-scales, i.e. 10 and 100 Myr in the HORIZON-AGN simulation, and we find that this does not change our conclusions.

[9] We checked that these values are correlated with those obtained from the stellar particles computed over a time-scale between 50 to 100 Myr.

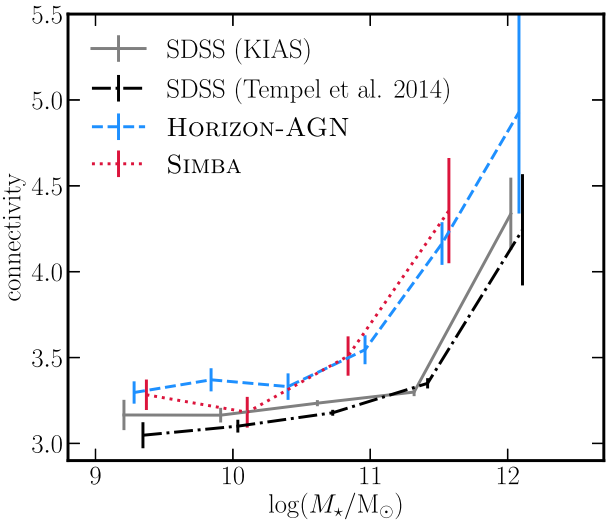

Figure 3. Mean connectivity as a function of $M_\star$ in the SDSS (solid grey line), Horizon-AGN (dashed blue line), and Simba (dotted red line). In order to quantify our uncertainties, we also use the Tempel et al. (2014) SDSS catalogue (dash–dotted black line). Both sets of simulations and postprocessing of the raw SDSS data from both catalogues yield consistent measurements. Connectivity increases with increasing $M_\star$ in qualitative agreement between observations and simulations. The residual difference in amplitude is driven by sampling at a fixed persistence (see Appendix A).

uncertainties, we also use the Tempel et al. (2014) SDSS catalogue[10] (dash–dotted black line) and find no significant differences.

The residual difference in the amplitude of the measured connectivity between the simulations and observations is driven by sampling at a fixed persistence and the difference in the mean number density in both data sets.[11] Indeed, if the matter density field is better sampled with a more complete catalogue, more filaments will be recovered at a given persistence (see Appendix A for more details).

We also note that the elbow in the connectivity–$M_\star$ relation, below which there is only a weak trend, happening near 5×10^{11} M$_\odot$, corresponds to the Press–Schechter mass of non-linearity $M_*(z = 0)$ times the baryon fraction, reflecting the transition between fully non-linear satellites and centrals that have collapsed recently (cf. Appendix B, Fig. B1).

Fig. 4 shows the connectivity averaged over galaxies in bins of $M_\star$ for populations with different star formation activities and morphologies. In each panel, the black solid line shows the mean connectivity for all galaxies at a fixed mass. In the top panel of Fig. 4, we distinguish between passive and star-forming galaxies (see Section 2.1). At a fixed stellar mass, passive galaxies (red line) tend to have higher connectivity than star-forming galaxies (blue line). In turn, when splitting galaxies by their morphological type (bottom panel), E/S0 galaxies (red line) are found to have higher connectivity than S/Irr galaxies (blue line) of the same $M_\star$. Although the redshift range is different, this finding is consistent with Darragh Ford et al. (2019), who investigated the link between connectivity, group mass, and the properties of the brightest group galaxy at a fixed group mass. Note that for passive/elliptical galaxies, there seems to be a bimodality in the distribution of connectivity and stellar mass, as revealed by the non-monotonicity of the red curve on both panels of Fig. 4. In particular, we tend to see a first bump at low mass and a second rise at larger mass. This is due to the two quite distinct populations of passive ellipticals: low-mass satellites, on the one hand, and massive centrals, on the other hand, which may, respectively, drive the low- and high-mass behaviours (see Appendix B).

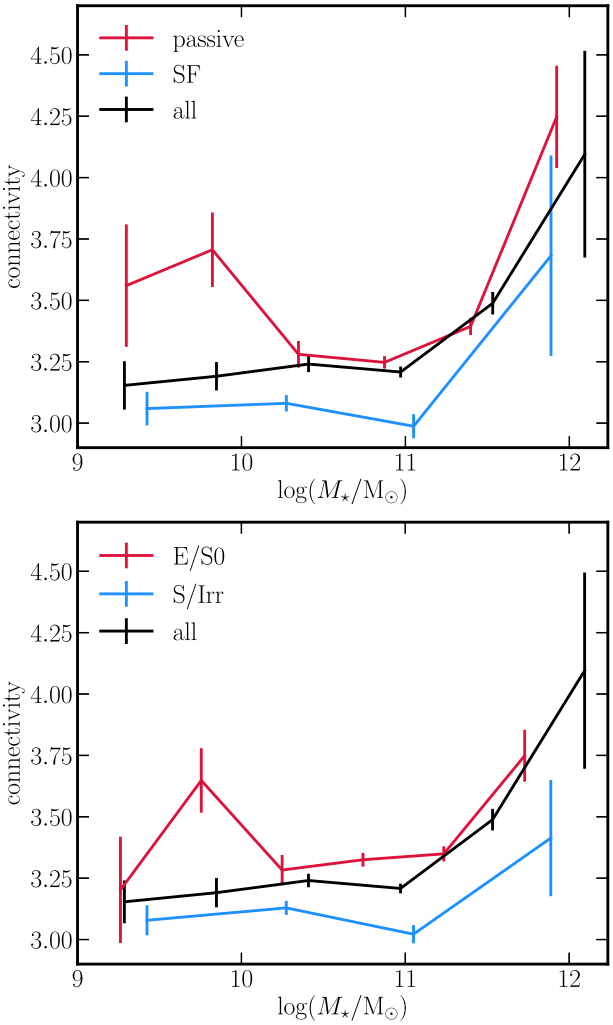

Figure 4. Mean connectivity as a function of stellar mass for different galaxy populations in the SDSS. The top panel shows results for the split by star formation activity of galaxies and the bottom panel shows results for the split by their morphology. Black solid line in each panel shows the mean connectivity for all galaxies at a fixed mass. More massive galaxies are found to have higher connectivity than their lower stellar mass counterparts. Passive or E/S0 type galaxies (red lines) have higher connectivity than star-forming or S/Irr type galaxies (blue lines) at the same $M_\star$.

3.2 sSFR dependence

It is well-known that the colour distribution of galaxies in the local Universe is bimodal (e.g. Strateva et al. 2001; Baldry et al. 2004; Brammer et al. 2009), with red galaxies dominated by massive quiescent spheroids, and blue galaxies being typically lower mass

[10]For the reconstruction of the cosmic web, coordinates corrected for the Fingers-of-God effect have been used.

[11]The mean galaxy number density in the SDSS at $z \leq 0.19$ is 4.4×10^{-3} Mpc^{-3}, while it is 1.3×10^{-1} and 4.9×10^{-2} $(h^{-1}$ Mpc$)^{-3}$ in the Horizon-AGN and Simba simulations at $z = 0$, respectively.

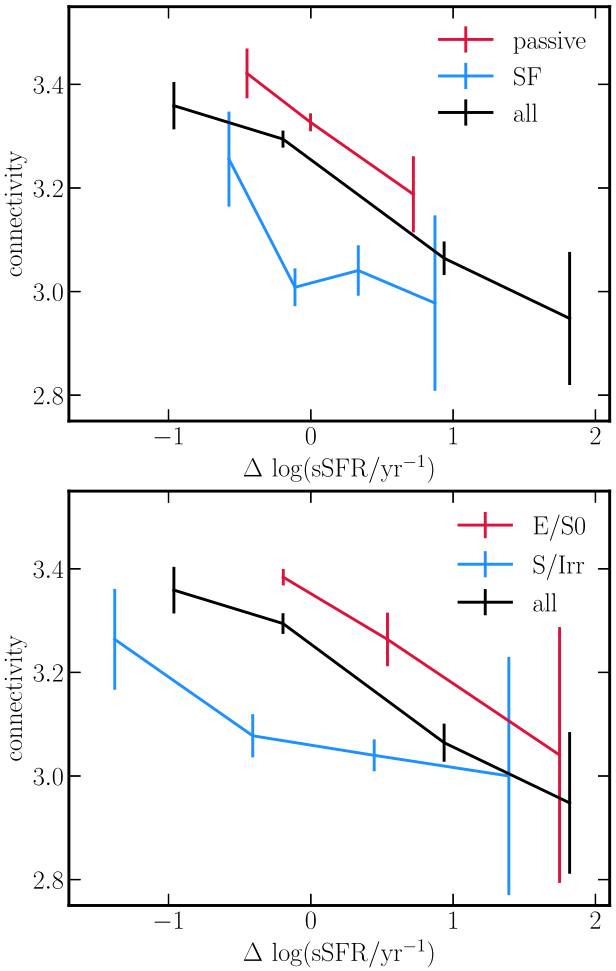

Figure 5. Mean connectivity as a function of the excess of sSFR at a given stellar mass for SDSS galaxies. The top panel shows results for the split by star formation activity of galaxies and the bottom panel shows results for the split by their morphology. The black solid line in each panel shows the mean connectivity for all galaxies. Both passive and star-forming galaxies with higher (lower) connectivity tend to have lower (higher) sSFR than the average at a fixed $M_\star$ of a given population. At a fixed sSFR excess, passive galaxies tend to be more connected than star-forming ones. Similarly, both elliptical/S0 and spiral/irregular galaxies with higher (lower) connectivity tend to have lower (higher) sSFR than the average at a fixed $M_\star$ of a given population. At a fixed sSFR excess, elliptical/S0 galaxies tend to be more connected than galaxies with spiral/irregular morphology.

star-forming discs (e.g. Kauffmann et al. 2003b; Balogh et al. 2004; Moustakas et al. 2013).

In order to account for this colour/sSFR – or morphology type– $M_\star$ dependence, Fig. 5 shows the connectivity as a function of excess sSFR at a given stellar mass, $\Delta\log\,(\mathrm{sSFR/yr^{-1}})$. The excess is computed at a fixed stellar mass with respect to the mean value of a given sub-population of galaxies. This allows us to probe the correlation between galaxy sSFR/type and connectivity beyond what is driven by stellar mass. We find that galaxies with higher connectivity tend to have lower sSFR than the average at the same $M_\star$, while those with lower connectivity have higher sSFR.

When splitting galaxies by their star formation activity (top panel of Fig. 5), both passive and star-forming galaxies are found to follow qualitatively similar trends for connectivity as a function of the excess sSFR, compared to what is found for the entire population. In addition, passive galaxies tend to have higher connectivity than star-forming galaxies at a fixed sSFR excess.

When splitting galaxies by their morphology type (bottom panel of Fig. 5), E/S0 galaxies are found to follow qualitatively similar trends for connectivity as a function of the excess sSFR to the entire galaxy population, i.e. E/S0 galaxies with a reduced sSFR at a fixed $M_\star$ have higher connectivity than E/S0 galaxies showing an excess in sSFR. S/Irr galaxies show a similar, albeit weaker, dependence in the connectivity–$\Delta\log\,(\mathrm{sSFR/yr^{-1}})$ parameter space. S/Irr galaxies that have lower sSFR compared to the average at the same $M_\star$ have higher connectivity compared to those with a positive sSFR excess that are (within the error bars) consistent with no dependence on the number of connected filaments. However, S/Irr galaxies tend to have lower connectivity than E/S0 galaxies, whatever be their sSFR excess (apart from the highest ΔsSFR bin with low statistics, where the two galaxy populations are within the error bars indistinguishable). The relative difference between passive and star-forming populations could be partly driven by the difference in stellar mass distributions of passive and star-forming galaxies, and E/S0 and S/Irr galaxies. Passive galaxies tend to be more massive than star-forming galaxies; they are, thus, expected to have on average higher connectivity compared to their star-forming counterparts. Similarly, for the E/S0 and S/Irr split, if E/S0s are more massive than S/Irr galaxies, the relative difference in connectivity can be driven by the underlying stellar mass dependence of connectivity.

What is more interesting is that once the sSFR dependence on stellar mass is accounted for, there is still a clear connectivity dependence for all galaxy populations, regardless of their morphology or star formation activity, such that galaxies with a large sSFR excess tend to have lower connectivity compared to galaxies with a larger sSFR deficit.

4 COMPARISON TO SIMULATIONS

This section presents measurements of connectivity in the HORIZON-AGN simulation. We note that qualitatively similar results are obtained in the SIMBA simulation, albeit with larger uncertainties (see Appendix D). The cosmic web is reconstructed as in the SDSS data, using galaxies as tracers of the matter distribution. Note that we use the HORIZON-AGN and SIMBA simulations as a reference for the measurement of the connectivity in a large-scale 'full-physics' experiment and not as an SDSS-like mock catalogue, given the large difference in volume and completeness. Section 4.1 recovers the scaling with stellar mass, while Section 4.2 investigates the effect of sSFR at a fixed mass on connectivity.

As for observational data (Section 3), we choose 3σ as a fiducial value for the persistence threshold used for the cosmic web reconstruction, even though the volume and sampling are quite different in the simulations. We have checked that similar results are obtained when different values are used, though when increasing N_σ to 5 and above, the number of galaxies identified as peaks of the cosmic web is dramatically reduced, making a statistical study less reliable. The histogram of the connectivity and multiplicity in the HORIZON-AGN and SIMBA simulations is shown in Fig. 2, with median values of 3 and 2, respectively, in very good agreement with values measured in observational data. The mean values are fairly similar, 3.41 ± 0.03 and 2.37 ± 0.02, for connectivity and multiplicity, respectively, in HORIZON-AGN, and 3.51 ± 0.06 and 2.36 ± 0.03, for connectivity and multiplicity, respectively, in SIMBA, again in agreement with measured values in the SDSS.

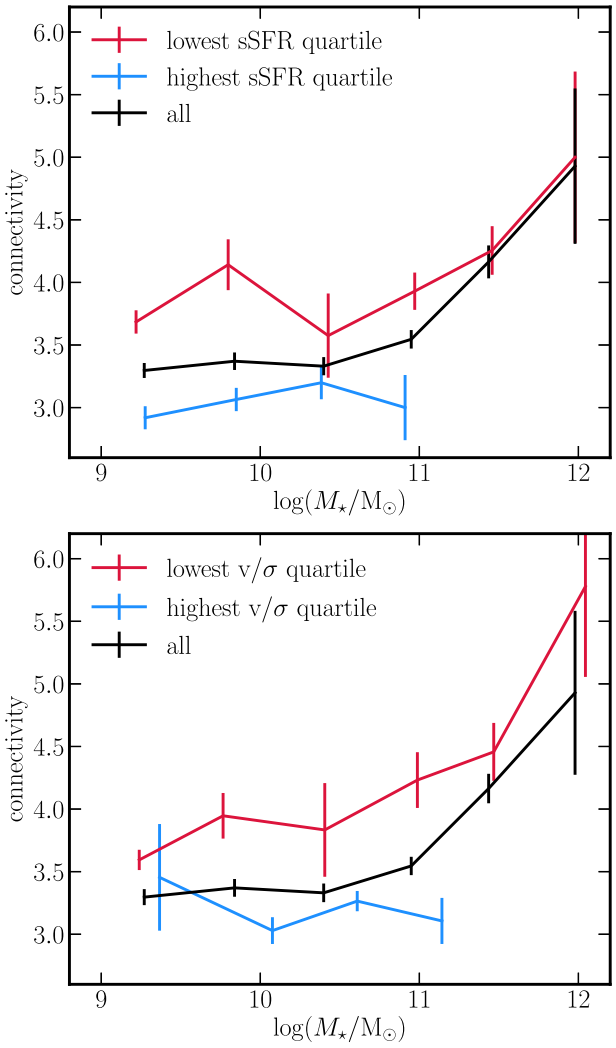

Figure 6. Mean connectivity as a function of stellar mass for different galaxy populations in HORIZON-AGN. The top panel shows results for the split by star formation activity of galaxies and the bottom panel shows results for the split by their morphology. Black solid line in each panel shows the mean connectivity for all galaxies at a fixed mass. More massive galaxies are found to have higher connectivity than their lower stellar mass counterparts. Galaxies with low sSFR or ellipticals (red lines) have higher connectivity than star-forming or disc-dominated galaxies (blue lines) at the same $M_\star$, in agreement with trends in the SDSS (see Fig. 4). The bump at $\sim 10^{10}$ M$_\odot$ for galaxies with low sSFR, also seen in the observations for passive galaxies (see Fig. 4), corresponds to satellites (see Appendix B).

The scaling with the threshold value N_σ for the cosmic web extraction is qualitatively similar to the one measured in the SDSS in Section 3 (see Table A1 in Appendix A).

4.1 Stellar mass dependence

Fig. 6 shows the stellar mass dependence of the connectivity in the HORIZON-AGN simulation, for populations with different star formation activities and morphologies. Black lines show connectivity at a given stellar mass for the entire galaxy population, reproducing the trends from Fig. 3 and in agreement with observations (see Fig. 4).

When splitting by star formation activity (top panel), galaxies with low sSFR (red line) at a fixed stellar mass tend to have higher connectivity than galaxies with high sSFR (blue line). We note that in the simulation we consider the lowest and highest sSFR quartiles, while in the observational data, we adopted a split into passive and star-forming galaxies (see Section 2.1). When we apply the same strategy on the SDSS data, i.e. sSFR quartiles, we obtain even better agreement with the simulations, in particular at high $M_\star$.[12]

In turn, when splitting galaxies by their morphological type (bottom panel), parametrized by v/σ, ellipticals (red line) are found to have higher connectivity than disc-dominated galaxies (blue line) of the same $M_\star$. This trend is again in agreement with measurements in observational data (see Fig. 4).

4.2 sSFR dependence

As we did for observations, in order to account for the underlying sSFR – and galaxy type–$M_\star$ relation, we study connectivity as a function of the excess sSFR at a given stellar mass. The result for the entire population of galaxies is shown in Fig. 7 (black line). Galaxies with higher connectivity tend to have lower sSFR than the average at the same $M_\star$, while those with lower connectivity have higher sSFR, once again in agreement with observations (see Fig. 5).

When splitting galaxies by their star formation activity (top panel of Fig. 7), both low- (red line) and high-sSFR (blue line) galaxies are found to follow qualitatively similar trends for connectivity as a function of the excess sSFR, compared to that found for the entire population. In addition, galaxies with low sSFR tend to have higher connectivity than galaxies with high sSFR at a fixed sSFR excess.

When splitting galaxies by morphology (bottom panel of Fig. 7), ellipticals (red line) are found to follow a qualitatively similar trend in sSFR versus connectivity as the entire galaxy population, i.e. elliptical galaxies with reduced sSFR at a fixed $M_\star$ have higher connectivity than ellipticals showing an excess in sSFR. Disc-dominated galaxies (blue line) do not show a strong dependence in the connectivity–$\Delta\log$ (sSFR/yr^{-1}) parameter space. Discy galaxies that have higher sSFR compared to the average at the same $M_\star$ have lower connectivity, compared to those with a negative sSFR excess that are (within the error bars) consistent with no dependence on the number of connected filaments. Note also that contrary to observations, the range of $\Delta\log$ (sSFR/yr^{-1}) values for disc galaxies is tighter. This is likely an effect of fairly low resolution that tends to oversmooth the SFR.

However, disc-dominated galaxies tend to have lower connectivity than elliptical galaxies, whatever their sSFR excess (in the range of values that have in common).

Overall, once the sSFR dependence on stellar mass is accounted for, there is still a clear connectivity dependence for all galaxy populations, regardless of their morphology or star formation activity, such that galaxies with a large sSFR excess tend to have lower connectivity compared to galaxies with a larger sSFR deficit, in agreement with the trends found in observations.

5 DISCUSSION

Let us now reframe the results of the previous section in terms of the underlying physical parameters, in order to disentangle the known effect of the halo mass (effectively the depth of the potential well of the host halo) from the environment (here the connectivity) on

[12]We choose to stick with the passive/star-forming split in the observations for its more common usage in the literature.

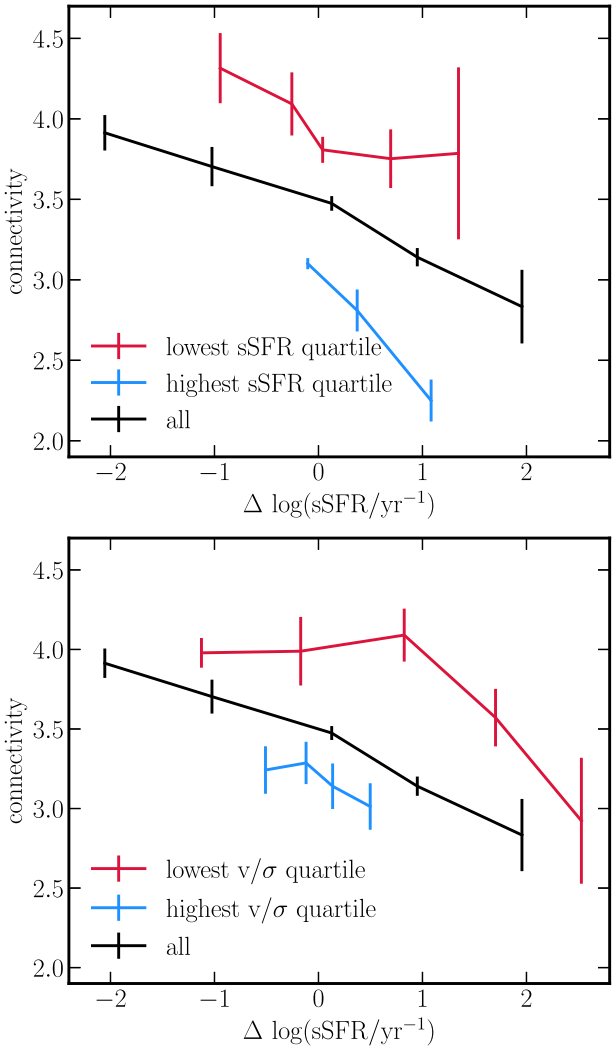

Figure 7. Mean connectivity as a function of the excess of sSFR at a given stellar mass in HORIZON-AGN. The top panel is split by star formation activity, while the bottom panel is split by morphology. Black solid line in each panel shows the mean connectivity for all galaxies. Both passive (red line) and star-forming (blue line) galaxies with higher (lower) connectivity have lower (higher) sSFR than the average, at a fixed $M_\star$ of a given population. At a fixed sSFR excess, galaxies with low sSFR are more connected than star-forming ones. Similarly, both ellipticals (red line) and disc-dominated (blue line) galaxies with higher (lower) connectivity have lower (higher) sSFR than the average at a fixed $M_\star$ of a given population. At a fixed sSFR excess, ellipticals are more connected than discy galaxies. Overall, galaxies with higher connectivity have lower sSFR than the average population at the same $M_\star$, regardless of their morphology or star formation activity, in agreement with trends seen in observations (see Fig. 5).

galaxy properties (Section 5.1). We will also quantify the effect of AGN feedback by comparing the measured connectivity in simulations with and without AGN feedback (Section 5.2). Finally, we will discuss connectivity versus other environmental tracers (Section 5.3).

5.1 Impact of halo mass

We start by addressing host halo mass, M_h, and its impact on the physical properties of galaxies in the framework of connectivity. Fig. 8, top panels, shows the evolution of connectivity as a function of main halo mass for, respectively, low and high stellar mass, sSFR, and v/σ in the HORIZON-AGN simulation. Connectivity increases with increasing halo mass. At a fixed M_h, galaxies with higher $M_\star$, lower sSFR, and lower v/σ tend to have higher connectivity compared to their lower mass, more star forming, and disc-dominated counterparts. This clearly shows that properties of galaxies are correlated with connectivity beyond halo mass. In addition, the trend is stronger for sSFR and v/σ compared to $M_\star$, suggesting an effect beyond that of halo and stellar mass.

Naively, one could expect, at least at high redshift, that at a given halo mass more connected galaxies would be fed by more cold gas, hence be more massive and star forming. One could also argue that a galaxy embedded in a single filament would be fed more coherent angular momentum, hence be more disc dominated. At lower redshift, the net effect of higher connectivity is less obvious since cosmic filaments may not reach down to galaxies, while less frequent minor mergers along the connected filaments may be dryer. In practice, at high mass, the opposite trend is observed at $z = 0$ (top panels of Fig. 8), i.e. more connected galaxies tend to have lower sSFR and v/σ.[13]

5.2 Impact of AGN feedback

Relying on the companion simulation HORIZON-NOAGN, the origin of this reversal can be pinned down in part on the impact of AGN feedback. As can be seen in bottom panels of Fig. 8, in the absence of AGN feedback, at low halo mass ($M_h \lesssim 10^{13}\mathrm{M}_\odot$), the connectivity between lowest and highest sSFR quartiles, on the one hand, and (to a lesser extent) lowest and highest v/σ quartiles, on the other hand, is consistent within the error bars. However, at high halo mass, the highest $M_\star$ quartile displays significantly higher connectivity than the lowest $M_\star$ quartile. We suggest that this is a consequence of the past effect of connectivity on building-up the stellar mass through gas accretion. Such a trend is not seen for sSFR, which is a more instantaneous quantity, because at low redshift additional quenching processes (e.g. gas shock heating) are likely to overcome the positive impact of connectivity. When AGN feedback is included, however, there is a clear correlation between high connectivity and passive/elliptical type. At high redshift, one could indeed expect that the higher gas mass load in more connected galaxies might boost the AGN activity, which, in turn, significantly contributes to the quenching and morphological change of galaxies (e.g. Dubois et al. 2013, 2016; Pontzen et al. 2017). Indeed, for centrals, AGN feedback quenches star formation by preventing the disc to reform. For satellites, it heats their host halo and contributes to starvation of their cold gas, hence quenching star formation (Dashyan et al. 2019). In this scenario, the residual dispersion in physical properties at a fixed halo mass is driven by connectivity, while the ordering (higher connectivity yields higher stellar mass, lower sSFR, and lower v/σ) is driven by AGN feedback at the high-mass end.

Although this interpretation is appealing, one could also speculate that there is no causation between connectivity and important quenching/morphological changes, but that both are driven by the same external cause. Interestingly, our results are qualitatively

[13] We note that we do not separate here between the centrals and satellites, which can be seen on the top left-hand panel, where the difference at a fixed high M_h is driven by the population of satellites. For the two remaining properties (sSFR and v/σ), splitting between centrals and satellites yields qualitatively similar results as for the entire population of galaxies.

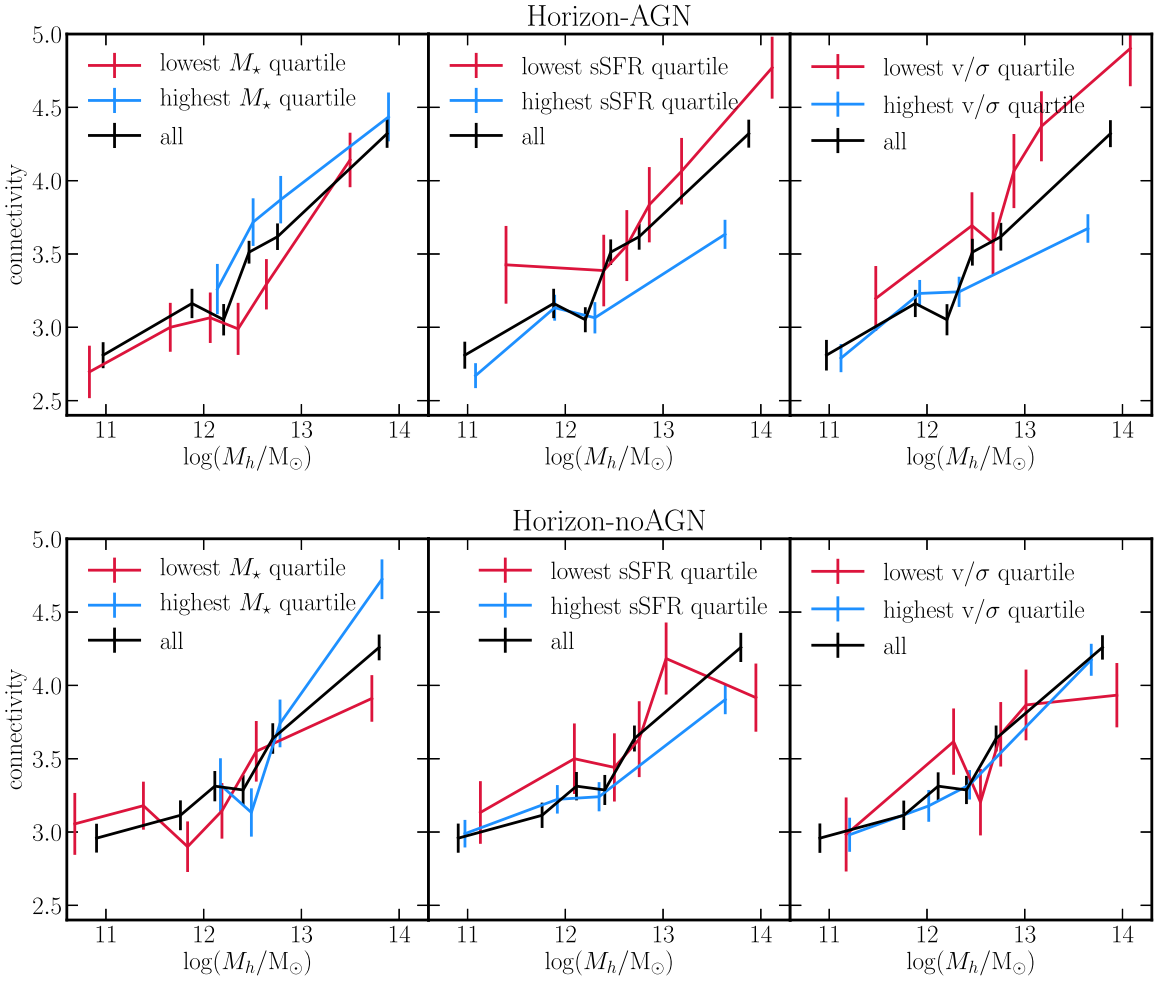

Figure 8. Mean connectivity as a function of halo mass in HORIZON-AGN (top panels). The left-hand panel shows results for the split by $M_\star$, the middle panel for the split by star formation activity, and the right-hand panel for the split by morphology. At a fixed halo mass, galaxies with higher $M_\star$, lower sSFR , and lower v/σ tend to have higher connectivity. Beyond halo mass, connectivity directly impacts galactic properties. Bottom panels show the same quantities for HORIZON-NOAGN. At all but highest M_h, no significant difference in connectivity is seen as a function of explored galaxy properties. At highest halo mass, there is a hint for reversal (or flattening) of the trend compared to HORIZON-AGN (strongest for $M_\star$ and v/σ).

consistent with the higher redshift findings of Darragh Ford et al. (2019), whereby more massive groups have higher *multiplicity*. From the analysis of the HORIZON-AGN light cone, they found that AGN feedback quenching efficiency is higher in more connected groups and that the highest multiplicity groups at a given group mass are very likely to be the result of a recent major merger. They suggested that a major merger, while increasing the net connectivity of the group (as long as each progenitor has a connectivity higher than 2), might also enhance black hole growth, boosting the AGN feedback strength, and therefore quenching the galaxy as a whole (e.g. Di Matteo, Springel & Hernquist 2005; Springel 2005; Dubois et al. 2016).

In fact, it is likely that both the above-described effects are at play. They could possibly be disentangled by looking at the redshift evolution of the trend, since the respective importance of mergers and smooth accretion in building up a massive halo mass will be a function of redshift. In order to verify that higher connectivity brings more cold gas to the galaxy, one could, in particula,r reproduce the same measurement in HORIZON-NOAGN at $z > 2$, where cold accretion is supposed to be very efficient. We will address this in future work.

As a final note, the qualitative agreement between our work and Darragh Ford et al. (2019) implies that in this regime, the global connectivity captures well enough local multiplicity around groups. It also suggests that there is no significant change in connectivity between redshift 0 and 1.

5.3 Connectivity versus other environment tracers

Let us briefly discuss the pros and cons of connectivity compared to traditional environment tracers. Density corresponds to number counts divided by the cube of some given scale, L. Connectivity naturally defines L as the typical distance from nodes to saddle points along the cosmic web. As such, connectivity is parameter free for a given skeleton.[14] Connectivity traces specifically the matter along filaments, where both the gas and satellite galaxies flow,

[14]Connectivity does depend on the persistence level chosen and on the sparsity of the catalogue – see Appendix A, but the level of persistence should in practice be effectively set near $N_\sigma = 3$ – unless one is attempting to match catalogues of distinct completeness.

whereas classical estimators, such as the fifth nearest neighbour, lose track of loci in the large-scale structures (the density ranges covered by walls and filaments, or filaments and nodes, overlap to some extent) and are only concerned with the isotropic effect of the environment. Conversely, the number of saddle points paired to a given maximum is determined by the topology of the local cosmic web. Connectivity is therefore a topologically robust[15] estimate, which captures the coherence of inflow along preferred directions. The robustness of connectivity is to be contrasted to the many existing definitions of the (isotropically averaged) local density. Formally, the dynamical state of a galaxy, which impacts directly its kinematics and morphology, reflects the past and present tides it was subjected to (in its past light cone), together with the baryonic processes operating within. Since gas shocks isothermally in many galactic circumstances, density ridges are paramount in defining both these tides and the loci of cold flow accretion. Connectivity is probably the simplest and most straightforward topological quantity capturing the effect of such ridges.

Note, finally, that this paper focused on the environment of galaxies at the *nodes* of the cosmic web, from which several filaments are branching out. Alternative metrics one could rely on in studying galaxy properties could be the distance to the closest filament (e.g. Alpaslan et al. 2016; Chen et al. 2017; Kleiner et al. 2017; Malavasi et al. 2017; Poudel et al. 2017; Crone Odekon et al. 2018; Kraljic et al. 2018; Laigle et al. 2018), distance to the closest wall (Kraljic et al. 2018), or 3D neighborhood of filaments in the frame of the saddle points (Kraljic et al. 2019). These studies typically also point towards an efficient mechanism that quenches star formation and transforms central galaxy morphology from late to early types.

6 CONCLUSIONS

We investigated the impact of the connectivity of the cosmic web on the properties of galaxies using the SDSS (via the MPA and KIAS value-added catalogues) and confronted those measurements to predictions from cosmological hydrodynamical simulations HORIZON-AGN, HORIZON-NOAGN, and SIMBA, while disentangling the effect of environment, AGN feedback, and mass. Our main results are as follows:

(i) The stellar mass dependence of connectivity and multiplicity is in qualitative agreement with theoretical predictions and measurements in dark matter simulations, once we account for the population of satellites.

(ii) The stellar mass, star formation activity, and morphology of galaxies all show some dependence on the connectivity (and multiplicity) of the cosmic web. More massive, less star forming, and less rotation supported galaxies tend to have higher connectivity.

(iii) These results qualitatively hold both for observed SDSS galaxies and HORIZON-AGN or SIMBA virtual galaxies. In the simulations, the connectivity at a fixed halo mass is higher for quenched, low-v/σ, more massive galaxies, which suggests that increasing the number of connected filaments reduces star formation and coherent angular momentum acquisition. This likely originates from filamentary-driven AGN activity, which quenches star formation and prevents disc reformation.

(iv) The publicly available code DISPERSE provides a flexible, robust, and physically motivated tool (via the connectivity) to quantify the observed geometry of galactic (anisotropic) environment.

This work underlines the importance of the anisotropic large-scale environment – traced by connectivity – in modulating galaxy properties beyond halo mass.

Future large-field spectroscopic surveys, such as 4MOST (de Jong et al. 2012), and photometric surveys, such as *Euclid* (Laureijs et al. 2011), HSC (Aihara et al. 2018), and LSST (LSST Dark Energy Science Collaboration 2012), will be able to confirm and extend these results by probing a wider group mass range and a larger variety of environment (though in 2D) while relying on state-of-the art photometric redshift extraction techniques (e.g. Davidzon et al. 2019; Pasquet et al. 2019).

Beyond the scope of this paper, it would be of interest to investigate the mass load and the wetness of the accretion *per filament* (as dry minor mergers would not contribute to the sSFR). One should also study how angular momentum is advected as a function of filament strength (Pichon et al. 2011), or consider the importance of the percolated geometry of the hot bubbles, as it will likely impact the quenching of satellites in the vicinity of nodes. One should also study the cosmic evolution of connectivity with redshift.[16] The redshift range of study can be broadened through Lyman α tomography (e.g. Lee et al. 2014, to probe $2 < z < 3.5$) or intensity mapping at higher redshifts (e.g. Chang et al. 2010), following individual haloes, or for the whole population at a given redshift, as the level of accretion required to trigger star formation activity is very redshift-dependent. This will be the topic of future work.

ACKNOWLEDGEMENTS

We thank Elmo Tempel for suggestions that helped to improve the presentation. KK thanks Joanne Cohn for fruitful discussions and helpful comments. SC is partially supported by a research grant from Fondation MERAC. CL and JD acknowledge funding support from Adrian Beecroft and the STFC. We thank S. Rouberol for smoothly running the HORIZON cluster for us and T. Sousbie for his help with DISPERSE, which is available at the following URL: www2.iap.fr/users/sousbie/disperse. We thank Stephen Appleby for fruitful comments and discussions while this work was carried out. We also thank Daniel Anglés-Alcázar and Desika Narayanan for helpful discussions. SIMBA was run on the DiRAC@Durham facility managed by the Institute for Computational Cosmology on behalf of the STFC DiRAC HPC Facility. The equipment was funded by BEIS capital funding via STFC capital grants ST/P002293/1, ST/R002371/1, and ST/S002502/1, Durham University, and STFC operations grant ST/R000832/1. DiRAC is part of the National e-Infrastructure. Funding for the SDSS and SDSS-II has been provided by the Alfred P. Sloan Foundation, the Participating Institutions, the National Science Foundation, the U.S. Department of Energy, the National Aeronautics and Space Administration, the Japanese Monbukagakusho, the Max Planck Society, and the Higher Education Funding Council for England. The SDSS web site is http://www.sdss.org/. The SDSS is managed

[15]It is strictly invariant for any monotonic local transformation of the field. It is also invariant with respect to continuous deformations, such as stretching, twisting, crumpling, and bending. It is also statistically robust, because it is fairly insensitive to shot noise, which impacts more strongly, e.g. nearest neighbours than the number of saddle points (Sousbie et al. 2011).

[16]Change in connectivity is a measure of a significant transformation of the field, which, as expected, also impacts properties of galaxies, which integrate past and present accretion.

by the Astrophysical Research Consortium for the Participating Institutions. The Participating Institutions are the American Museum of Natural History, Astrophysical Institute Potsdam, University of Basel, Cambridge University, Case Western Reserve University, University of Chicago, Drexel University, Fermilab, the Institute for Advanced Study, the Japan Participation Group, Johns Hopkins University, the Joint Institute for Nuclear Astrophysics, the Kavli Institute for Particle Astrophysics and Cosmology, the Korean Scientist Group, the Chinese Academy of Sciences (LAMOST), Los Alamos National Laboratory, the Max-Planck-Institute for Astronomy (MPIA), the Max-Planck-Institute for Astrophysics (MPA), New Mexico State University, Ohio State University, University of Pittsburgh, University of Portsmouth, Princeton University, the United States Naval Observatory, and the University of Washington.

REFERENCES

Abazajian K. N. et al., 2009, ApJS, 182, 543
Ahn C. P. et al., 2014, ApJS, 211, 17
Aihara H. et al., 2018, PASJ, 70, S4
Alpaslan M. et al., 2016, MNRAS, 457, 2287
Anglés-Alcázar D., Davé R., Faucher-Giguère C.-A., Özel F., Hopkins P. F., 2017, MNRAS, 464, 2840
Appleby S., Park C., Hong S. E., Kim J., 2017, ApJ, 836, 45
Aubert D., Pichon C., Colombi S., 2004, MNRAS, 352, 376
Baldry I. K., Glazebrook K., Brinkmann J., Ivezić, Ž., Lupton R. H., Nichol R. C., Szalay A. S., 2004, ApJ, 600, 681
Baldry I. K., Balogh M. L., Bower R. G., Glazebrook K., Nichol R. C., Bamford S. P., Budavari T., 2006, MNRAS, 373, 469
Balogh M. L., Baldry I. K., Nichol R., Miller C., Bower R., Glazebrook K., 2004, ApJ, 615, L101
Bamford S. P. et al., 2009, MNRAS, 393, 1324
Blanton M. R. et al., 2003, ApJ, 594, 186
Bond J. R., Kofman L., Pogosyan D., 1996, Nature, 380, 603
Brammer G. B. et al., 2009, ApJ, 706, L173
Brinchmann J., Charlot S., White S. D. M., Tremonti C., Kauffmann G., Heckman T., Brinkmann J., 2004, MNRAS, 351, 1151
Bruzual G., Charlot S., 2003, MNRAS, 344, 1000
Burton C. S. et al., 2013, MNRAS, 433, 771
Chang T.-C., Pen U.-L., Bandura K., Peterson J. B., 2010, Nature, 466, 463
Chen Y.-C. et al., 2017, MNRAS, 466, 1880
Choi Y.-Y., Han D.-H., Kim S. S., 2010, J. Korean Astron. Soc., 43, 191
Codis S., Pogosyan D., Pichon C., 2018, MNRAS, 479, 973
Crone Odekon M., Hallenbeck G., Haynes M. P., Koopmann R. A., Phi A., Wolfe P.-F., 2018, ApJ, 852, 142
Cucciati O. et al., 2010, A&A, 524, A2
Cucciati O. et al., 2017, A&A, 602, A15
Darragh Ford E. et al., 2019, MNRAS, 489, 5695
Dashyan G., Choi E., Somerville R. S., Naab T., Quirk A. C. N., Hirschmann M., Ostriker J. P., 2019, MNRAS, 487, 5889
Davé R., Thompson R., Hopkins P. F., 2016, MNRAS, 462, 3265
Davé R., Anglés-Alcázar D., Narayanan D., Li Q., Rafieferantsoa M. H., Appleby S., 2019, MNRAS, 486, 2849
Davidzon I. et al., 2019, MNRAS, 489, 4835
Davis M., Geller M. J., 1976, ApJ, 208, 13
de Jong R. S. et al., 2012, Proc. SPIE Conf. Ser., Ground-Based and Airborne Instrumentation for Astronomy IV, Vol. 8448. SPIE, Bellingham, p. 84460T
Dekel A. et al., 2009, Nature, 457, 451
de Lapparent V., Geller M. J., Huchra J. P., 1986, ApJ, 302, L1
Di Matteo T., Springel V., Hernquist L., 2005, Nature, 433, 604
Dressler A. et al., 1997, ApJ, 490, 577
Dressler A., 1980, ApJ, 236, 351
Dubois Y., Devriendt J., Slyz A., Teyssier R., 2012, MNRAS, 420, 2662
Dubois Y., Gavazzi R., Peirani S., Silk J., 2013, MNRAS, 433, 3297
Dubois Y. et al., 2014, MNRAS, 444, 1453
Dubois Y., Peirani S., Pichon C., Devriendt J., Gavazzi R., Welker C., Volonteri M., 2016, MNRAS, 463, 3948
Forman R., 2002, Sém. Lothar. Combin., 48, 35 (electronic)
Gay C., Pichon C., Le Borgne D., Teyssier R., Sousbie T., Devriendt J., 2010, MNRAS, 404, 1801
Goto T., Yamauchi C., Fujita Y., Okamura S., Sekiguchi M., Smail I., Bernardi M., Gomez P. L., 2003, MNRAS, 346, 601
Haardt F., Madau P., 1996, ApJ, 461, 20
Haardt F., Madau P., 2012, ApJ, 746, 125
Hashimoto Y., Oemler Augustus J., Lin H., Tucker D. L., 1998, ApJ, 499, 589
Hopkins P. F., 2015, MNRAS, 450, 53
Hwang H. S. et al., 2016, ApJ, 818, 173
Kauffmann G. et al., 2003a, MNRAS, 341, 33
Kauffmann G. et al., 2003b, MNRAS, 341, 54
Kauffmann G., White S. D. M., Heckman T. M., Ménard B., Brinchmann J., Charlot S., Tremonti C., Brinkmann J., 2004, MNRAS, 353, 713
Kennicutt R. C., Evans N. J., 2012, ARA&A, 50, 531
Kereš D., Katz N., Weinberg D. H., Davé R., 2005, MNRAS, 363, 2
Kereš D., Katz N., Fardal M., Davé R., Weinberg D. H., 2009, MNRAS, 395, 160
Kleiner D., Pimbblet K. A., Jones D. H., Koribalski B. S., Serra P., 2017, MNRAS, 466, 4692
Klypin A., Shandarin S. F., 1993, ApJ, 413, 48
Komatsu E. et al., 2011, ApJS, 192, 18
Kraljic K. et al., 2018, MNRAS, 474, 547
Kraljic K. et al., 2019, MNRAS, 483, 3227
Kroupa P., 2001, MNRAS, 322, 231
Krumholz M. R., Gnedin N. Y., 2011, ApJ, 729, 36
Laigle C. et al., 2016, ApJS, 224, 24
Laigle C. et al., 2018, MNRAS, 474, 5437
Larson R. B., Tinsley B. M., Caldwell C. N., 1980, ApJ, 237, 692
Laureijs R. et al., 2011, preprint (arXiv:1110.3193)
Lee K.-G., Hennawi J. F., Stark C., Prochaska e. a., 2014, ApJ, 795, L12
Lewis I. et al., 2002, MNRAS, 334, 673
Lintott C. et al., 2011, MNRAS, 410, 166
LSST Dark Energy Science Collaboration, 2012, preprint (arXiv:1211.0310)
Lynden-Bell D., 1964, ApJ, 139, 1195
Malavasi N. et al., 2017, MNRAS, 465, 3817
Moustakas J. et al., 2013, ApJ, 767, 50
Park C., Choi Y., 2005, ApJ, 635, L29
Park C., Choi Y.-Y., Kim J., Gott J. R., III, Kim S. S., Kim K.-S., 2012, ApJ, 759, L7
Pasquet J., Bertin E., Treyer M., Arnouts S., Fouchez D., 2019, A&A, 621, A26
Peirani S. et al., 2017, MNRAS, 472, 2153
Pichon C., Pogosyan D., Kimm T., Slyz A., Devriendt J., Dubois Y., 2011, MNRAS, 418, 2493
Planck Collaboration XIII, 2016, A&A, 594, A13
Pogosyan D., Pichon C., Gay C., Prunet S., Cardoso J. F., Sousbie T., Colombi S., 2009, MNRAS, 396, 635
Pontzen A., Tremmel M., Roth N., Peiris H. V., Saintonge A., Volonteri M., Quinn T., Governato F., 2017, MNRAS, 465, 547
Poudel A., Heinämäki P., Tempel E., Einasto M., Lietzen H., Nurmi P., 2017, A&A, 597, A86
Sarron F., Adami C., Durret F., Laigle C., 2019, MNRAS, 632, A49
Sousbie T., Pichon C., Kawahara H., 2011, MNRAS, 414, 384
Springel V., 2005, MNRAS, 364, 1105
Strateva I. et al., 2001, AJ, 122, 1861
Sutherland R. S., Dopita M. A., 1993, ApJS, 88, 253
Tegmark M. et al., 2004, ApJ, 606, 702
Tempel E. et al., 2014, A&A, 566, A1

Teyssier R., 2002, A&A, 385, 337
Thomas N., Davé R., Anglés-Alcázar D., Jarvis M., 2019, MNRAS, 487, 5764
Willett K. W. et al., 2013, MNRAS, 435, 2835
York D. G. et al., 2000, AJ, 120, 1579
Zel'dovich Y. B., 1970, A&A, 5, 84

APPENDIX A: IMPACT OF PERSISTENCE

Let us investigate briefly the impact of varying the persistence on connectivity. Recall that persistence controls the relative density of critical topologically paired points connected by the skeleton. As such, dropping lower persistence pairs ensures that only the most robust filaments are retained, should one want to focus on those. Since DisPerSE operates directly on the galaxy catalogues, their sparsity also impacts the scale at which filaments can be robustly extracted. Varying the level of persistence of the more complete catalogue provides means to match the less complete one.

Fig. A1 reproduces the PDF of connectivity shown in Fig. 2 for a level of persistence of $5N_\sigma$, in order to reflect the fact that the galactic sampling in the SDSS is much sparser than in the simulations. As expected, the agreement between the simulations and the observations is improved at that level of persistence, in particular for the low-connectivity bin. Similarly, Fig. A2 reproduces Fig. 3 for both simulations and the SDSS catalogue. One could, in principle, calibrate more precisely the persistence level to reflect the difference in density in both data sets. However, in the main text, we chose a lower persistence level of $3N_\sigma$ in order to avoid having too large error bars, given the much smaller volume of the simulation. We refer to Codis et al. (2018) for a more detailed investigation of the impact of persistence on connectivity and multiplicity.

Alternatively, one could create a subsample of galaxies from the simulations by matching the mean density in the SDSS. However, such a strategy is not feasible because of the small volume of the simulation. It would lead to a reduction in the number of galaxies by a factor of ∼10, which would severely impact the cosmic web reconstruction. Additionally, the overall statistics would become insufficient for the current analysis.

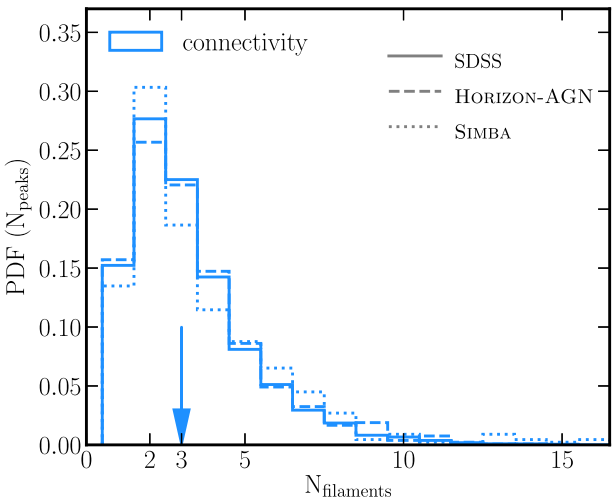

Figure A1. PDF of the connectivity in the SDSS (solid) at the persistence level $N_\sigma = 3$, and in Horizon-AGN (dashed) and Simba (dotted) at the persistence level $N_\sigma = 5$. The arrow shows the median of the distributions for all three data sets. Increased level of persistence in the simulations yields a better agreement with the observations, as it matches better the sampling of the observational data set.

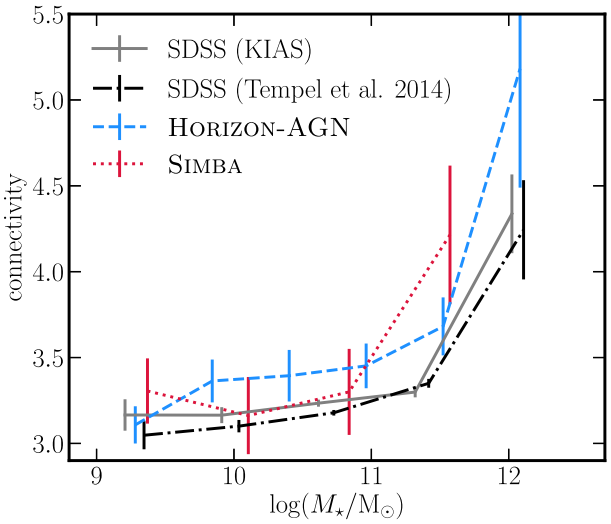

Figure A2. Mean connectivity as a function of $M_\star$ in the SDSS (solid grey) at the persistence level $N_\sigma = 3$, and in Horizon-AGN (dashed blue) and Simba (dotted red) at the persistence level $N_\sigma = 5$. Increased persistence in the simulations yields a better agreement with the observations at the expense of increased error bars.

Table A1. Mean, standard deviation, and 20th, 50th, and 80th percentiles for connectivity at different persistence levels N_σ in the SDSS, and simulations Horizon-AGN, Horizon-noAGN, and Simba.

	N_σ	Mean	std	Percentile		
				Median	20	80
SDSS	1	4	2.2	4	2	6
	3	3.3	2.0	3	2	5
	5	3.3	2.0	3	2	5
Horizon-AGN	1	4	2.2	4.1	2	6
	3	3.4	1.9	3	2	5
	5	3.4	2.1	3	2	5
Horizon-noAGN	1	4	2.2	4	2	5
	3	3.4	1.9	3	2	5
	5	3.4	2.2	3	2	5
Simba	1	4	2.2	4.1	2	6
	3	3.5	2.0	3	2	5
	5	3.6	2.5	3	2	5

Table A2. Mean, standard deviation, and 20th, 50th, and 80th percentiles for multiplicity at different persistence levels N_σ in the SDSS, and simulations Horizon-AGN, Horizon-noAGN, and Simba.

	N_σ	Mean	std	Percentile		
				Median	20	80
SDSS	1	3.3	1.3	3	2	4
	3	2.2	0.9	2	1	3
	5	1.7	0.7	2	1	2
Horizon-AGN	1	3.1	1.3	3	2	4
	3	2.4	0.96	2	2	3
	5	2.1	0.8	2	1	3
	1	3.1	1.3	3	2	4
	3	2.4	0.95	2	2	3
	5	2	0.81	2	1	3
Simba	1	3.1	1.3	3	2	4
	3	2.4	0.96	2	2	3
	5	1.96	0.8	2	1	3

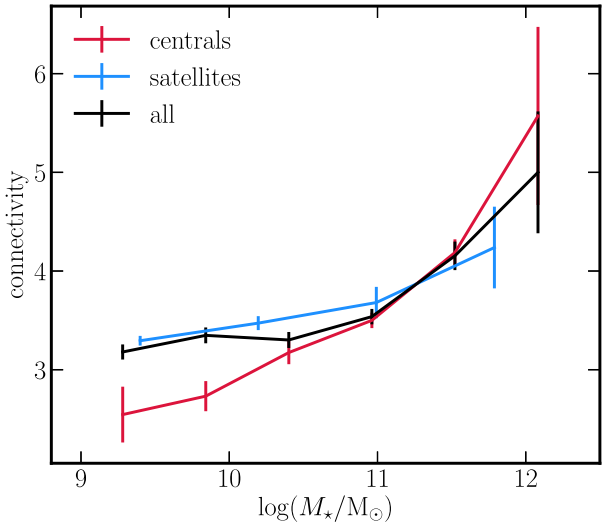

Figure B1. Mean connectivity as a function of $M_\star$ in HORIZON-AGN at the persistence level $N_\sigma = 3$ for centrals (in red), satellites (in blue), and the full population (in black). The agreement with the expected trend (increasing connectivity with increasing $M_\star$) is stronger for the central. The elbow of the full population near $M_\star = 10^{11}\mathrm{M}_\odot$ corresponds to the transition where it is dominated by satellites.

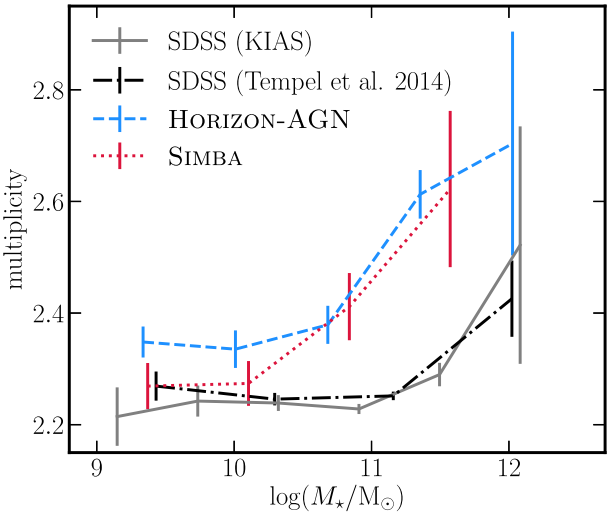

Figure C1. Mean multiplicity as a function of $M_\star$ in the SDSS (solid grey line), HORIZON-AGN (dashed blue line), and SIMBA (dotted red line). In order to quantify our uncertainties, we also use the Tempel et al. (2014) SDSS catalogue (dash–dotted black line). Both sets of simulations and post-processing of the raw SDSS data from both catalogues yield consistent measurements. Multiplicity increases with increasing $M_\star$ in qualitative agreement between observations and simulations, in qualitative agreement with the measured connectivity (see Fig. 3).

APPENDIX B: IMPACT OF SATELLITES

Let us briefly highlight the impact of the distribution of satellites on the connectivity–$M_\star$ relation presented in the main text. The lower mass (satellite) galaxies dominate in number the population near the nodes of the cosmic web. This population has lower connectivity than the centrals, hence creating an elbow in the connectivity–$M_\star$ relation for all galaxies, below which the connectivity shows only a weak dependence on $M_\star$. This is seen in Fig. B1, which plots the connectivity as a function of $M_\star$ for all galaxies (black line), centrals (red line), and satellites (blue line) in the HORIZON-AGN simulation. Globally, satellites do impact figures like Fig. 4, but for the sake of studying connectivity counts split by multiple physical parameters, we consider the full population in the main text.

APPENDIX C: MULTIPLICITY

Let us investigate the evolution of multiplicity with the physical parameters of connected galaxies. Multiplicity is complementary to connectivity, and is, in principle, a better proxy for the *local* mass load, as mentioned in Section 2.2. On the other hand, multiplicity explicitly depends on the length over which the skeleton is smoothed. It is, therefore, less parameter free than the connectivity. The range of values it takes is also narrower; hence, it provides less leverage over environment on larger scales (connectivity probes saddles points, which can be at some distance away from the nodes). It is also more complicated to predict from the first principle (the geometry of accretion involves N-point correlations of extrema around peaks, as discussed in Codis et al. 2018).

Fig. C1 shows the multiplicity averaged over galaxies in bins of $M_\star$ for the entire galaxy population in the two SDSS catalogues (solid grey and dash–dotted black lines), HORIZON-AGN (dashed blue line), and SIMBA (red dotted line). Multiplicity of galaxies is found to increase with increasing $M_\star$, in a qualitative agreement with the measured connectivity (see Fig. 3).

Figs C2 and C3 show the multiplicity as a function of the sSFR excess at a given stellar mass, $\Delta\log(\mathrm{sSFR/yr}^{-1})$, in HORIZON-AGN and the SDSS, respectively. Qualitatively similar trends to those obtained for the connectivity are found when splitting by sSFR and morphology (or v/σ in HORIZON-AGN), for both simulations and the observed data (see Figs 5 and 7).

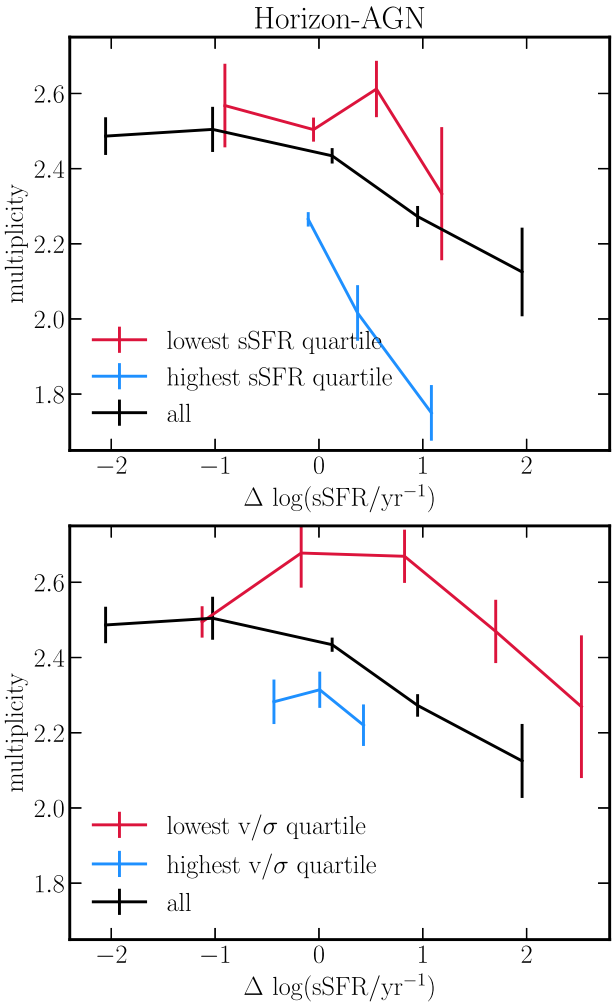

Figure C2. Mean multiplicity as a function of the excess of sSFR at a given stellar mass in HORIZON-AGN. The top panel is split by star formation activity, while the bottom panel by morphology. The black solid line in each panel shows the mean multiplicity for all galaxies. Both passive (red line) and star-forming (blue line) galaxies with higher (lower) multiplicity tend to have a lower (higher) sSFR than the average at a fixed $M_\star$ of a given population. At a fixed sSFR excess, galaxies with low sSFR tend to be more connected than star-forming ones. Similarly, both ellipticals (red line) and disc-dominated (blue line) galaxies with higher (lower) multiplicity tend to have lower (higher) sSFR than the average at a fixed $M_\star$ of a given population. At a fixed sSFR excess, ellipticals are more connected than spiral galaxies. Overall, galaxies with higher multiplicity have lower sSFR than the average population at the same $M_\star$, regardless of their morphology or star formation activity.

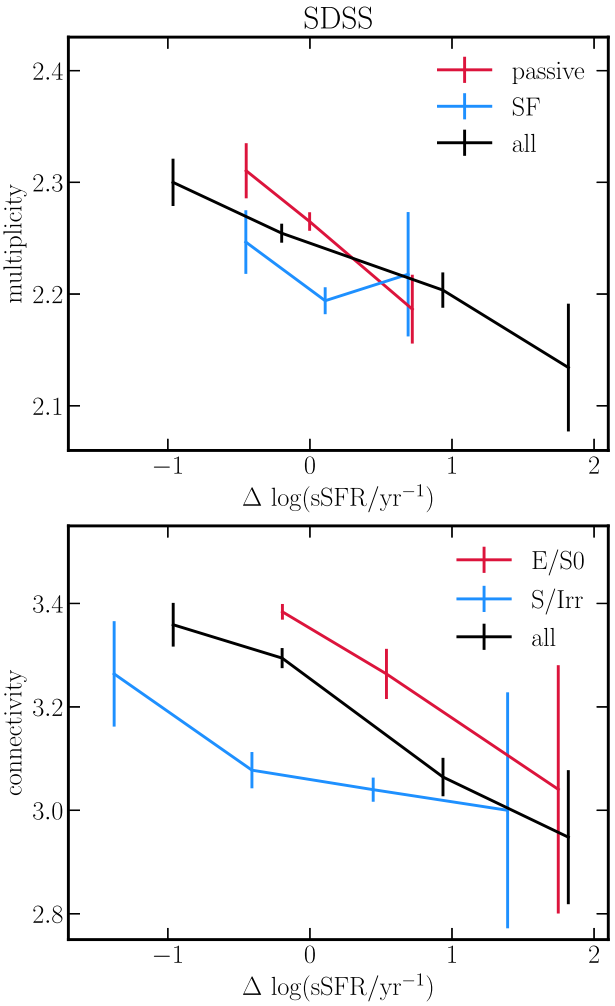

Figure C3. Mean multiplicity as a function of the excess of sSFR at a given stellar mass for SDSS galaxies. The top panel is split by star formation activity of galaxies, while the bottom panel by morphology. The black solid line in each panel shows the mean multiplicity for all galaxies. As in Fig. C2, both passive and star-forming galaxies with higher (lower) connectivity tend to have lower (higher) sSFR than the average at a fixed $M_\star$ of a given population. At a fixed sSFR excess, passive galaxies tend to be more connected (locally) than star-forming ones. Similarly, both elliptical/S0 and spiral/irregular galaxies with higher (lower) multiplicity tend to have lower (higher) sSFR than the average at a fixed $M_\star$ of a given population. At a fixed sSFR excess, elliptical/S0 galaxies tend to be more connected than galaxies with spiral/irregular morphology.

APPENDIX D: CONNECTIVITY IN SIMBA

We finally present in Fig. D1 the mean connectivity as a function of $M_\star$ (top panel) and sSFR excess at a fixed $M_\star$ (bottom panel) in the SIMBA simulation. Overall, the trends with sSFR are qualitatively similar to those obtained in the SDSS and HORIZON-AGN, albeit with larger uncertainties due to lower statistics. The variation in mean connectivity with excess sSFR is also flatter; however, at a fixed sSFR excess, galaxies with low sSFR continue to have higher connectivity than highly star-forming galaxies. The details of the baryonic physics modelling likely impact the measured trends. Assessing the origin of the differences is beyond the scope of this paper.

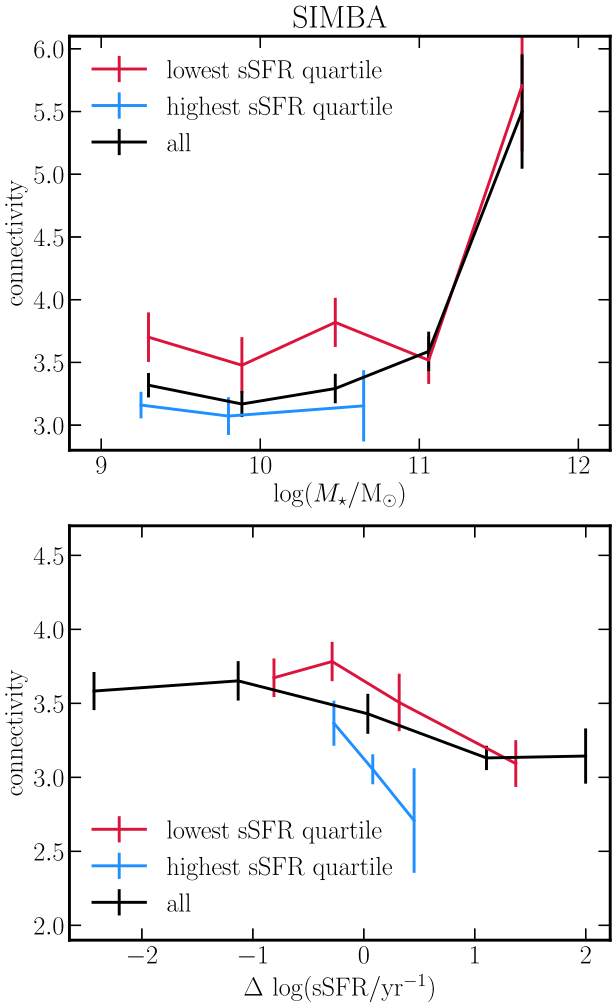

Figure D1. Mean connectivity as a function of $M_\star$ (top panel) and sSFR excess (bottom panel) for star-forming (blue lines) and passive (red lines) galaxies in SIMBA. The black solid line in each panel shows the mean connectivity for all galaxies at a fixed mass. Galaxies with low sSFR have higher connectivity than star-forming galaxies (blue lines) at the same $M_\star$, in agreement with trends in the SDSS (see Fig. 4) and HORIZON-AGN (see Fig. 6). Both passive and star-forming galaxies with higher (lower) connectivity have lower (higher) sSFR than average, at a fixed $M_\star$ of a given population. At a fixed sSFR excess, galaxies with low sSFR are more connected than star-forming ones. Overall, galaxies with higher connectivity have lower sSFR than the average population at the same $M_\star$, regardless of their star formation activity, in agreement with trends seen in observations (see Fig. 5) and HORIZON-AGN (see Fig. 7).

This paper has been typeset from a TEX/LATEX file prepared by the author.